Molecular Therapy
Nucleic Acids
Original Article

Modified ASO conjugates encapsulated with cytidinyl/cationic lipids exhibit more potent and longer-lasting anti-HCC effects

Yufei Pan,[1,4] Jing Guan,[2,4] Yujing Gao,[3] Yuejie Zhu,[1] Huantong Li,[1] Hua Guo,[1] Qianyi He,[1] Zhu Guan,[1] and Zhenjun Yang[1]

[1]State Key Laboratory of Natural and Biomimetic Drugs, School of Pharmaceutical Sciences, Peking University, Beijing 100191, China; [2]Key Laboratory of Plant Resource Conservation and Germplasm Innovation in Mountainous Region (Ministry of Education), College of Life Sciences/Institute of Agro-bioengineering, Guizhou University, Guiyang 550025, China; [3]School of Pharmacy, Chengdu University of Traditional Chinese Medicine, Chengdu 611137, China

Antisense oligonucleotides (ASOs) are a class of therapeutics targeting mRNAs or genes that have attracted much attention. However, effective delivery and optimal accumulation in target tissues *in vivo* are still challenging issues. CT102 is an ASO that targets *IGF1R* mRNA and induces cell apoptosis. Herein, a detailed exploration of the tissue distribution of ASOs delivered by liposomes was carried out. A formulation that resulted in increased hepatic accumulation was identified based on multiple intermolecular interactions between DCP (cytidinyl/cationic lipid DNCA/CLD and DSPE-PEG) and oligonucleotides, including hydrogen bonding, π-π stacking, and electrostatic interactions. The structurally optimized CT102s present a novel strategy for the treatment of hepatocellular carcinoma. The gapmer $CT102_{MOE5}$ and conjugate Glu-$CT102_{MOE5}$ showed superior antiproliferation and *IGF1R* mRNA suppression effects at 100 nM *in vitro* and achieved greater efficacy at a lower dose and administration frequency *in vivo*. Combined transcriptome and proteome analyses revealed that additional associated targets and functional regulations might simultaneously exist in ASO therapy. These results showed that a combination of lipid encapsulation and structural optimization in the delivery of oligonucleotide drugs has favorable prospects for clinical application.

INTRODUCTION

Oligonucleotides (ONs) are highly potent drug molecules that have been effectively used for the treatment of various diseases.[1–4] They act directly on mRNA and drastically inhibit *de novo* protein synthesis of a targeted gene through posttranscriptional gene silencing.[5] However, the transfection of ONs, especially the biological stability and precise delivery into the target tissue or respective cell types, has always been challenging.[6–8] Recently, a combination of chemical modifications, mainly to the phosphodiester linkage and 2'-ribose position, essentially resolved *in vivo* stability.[9] Various new delivery methods are emerging to enhance target tissue accumulation and cellular uptake.[10,11]

SNALP, represented by Onpattro, which hit the market in 2018, comprised the pH-sensitive ionizable lipid DLin-MC3-DMA, shielding lipid PEG-DMG, helper lipid DSPC, and cholesterol.[12,13] Onpattro is transported *in vivo* mainly through ApoE in the circulatory system and enters the cell via receptor-mediated pathways. Currently, essentially all clinical or research lipid materials are cationic liposomes.[14–17] Cationic lipids can efficiently encapsulate polyanionic ONs. Nevertheless, irreversible damage to cell membranes raises unavoidable toxicity issues. To achieve effective encapsulation, the proportion of cationic lipids relying solely on electrostatic interactions in the final formulation must be relatively high and immobilized. The factors affecting the *in vivo* distribution of ONs after lipid delivery have been relatively obscure.[18] On the basis of SNALP, Siegwart and co-workers[19,20] added SORT molecules with different structures to achieve tissue targeting. They correlated the tissue-targeting properties with the apparent pK_a of lipid nanoparticles (LNPs). After extensive screening, they obtained a pK_a-related tissue property distribution index with a high reference value. In addition to the lipid structure, the surface electrical properties of liposomes affect organ-specific distribution. LoPresti et al.[21] achieved efficient mRNA delivery to the spleen and lungs by replacing helper lipids with charged alternatives in LNPs. Unfortunately, lipid delivery research for ON drugs has not been as detailed as mRNA delivery research. Although there are some case reports of the delivery of ONs to extrahepatic tissues,[22] such as the lungs,[23] the specific mechanism has not been elucidated.

GalNAc conjugation, another novel strategy for biopharmaceutical innovation, has facilitated the production of four related drugs (givosiran, lumasiran, inclisiran, and vutrisiran).[24–26] This strategy

Received 12 December 2022; accepted 28 April 2023;
https://doi.org/10.1016/j.omtn.2023.04.028.

[4]These authors contributed equally

Correspondence: Zhenjun Yang, State Key Laboratory of Natural and Biomimetic Drugs, School of Pharmaceutical Sciences, Peking University, Beijing 100191, China.
E-mail: yangzj@bjmu.edu.cn

eliminates the need for lipid carriers since the GalNAc moiety can target the asialoglycoprotein receptor (ASGPR) on the surface of hepatocytes and mediate drug endocytosis.[27] This technology has become a mainstream strategy to achieve liver-targeting delivery of ONs and significantly reduces the dosing frequency to 1–6 months/time by s.c. administration.[28–30] In addition, it is not rare for other monosaccharide or polysaccharide molecules to target receptors on cell membranes for drug delivery.[31–33] Tumors exhibit enhanced glucose uptake to maintain their rapid cellular proliferation. Accordingly, Patra et al.[34] designed and synthesized a series of glucose-cisplatin conjugates to enhance uptake by tumor cells while reducing the toxic side effects of cisplatin drugs. Moreover, the mannose receptor is a critical pattern recognition receptor in the innate immune system, which is mainly present on the cell membrane surface of macrophages and dendritic cells. The development of mannose-related agents targeting this receptor is also a popular research topic.[35,36]

Herein, CT102 is a phosphorothioated deoxyoligonucleotide targeting the human insulin-like growth factor type 1 receptor (*IGF1R*) gene, which can effectively inhibit the proliferation of hepatocellular carcinoma (HCC) cells.[37] Previous studies have shown that DCP (cytidinyl/cationic mixed lipids, DNCA/CLD/DSPE-PEG, Table S1), a novel transfection system based on hydrogen bonding and π-π stacking, can deliver various ON drugs into cells with high efficiency.[38–43] The combined encapsulation effect of various intermolecular forces makes the ratio of the formulation components more flexible depending on the context, and the cationic lipid levels can be negligible. Compared with sorafenib, DCP-CT102 achieved greater efficacy at a dose of ∼2 mpk administered every other day.[44]

In this study, through the delivery of DCP lipids and adjustment of various formulation conditions, the optimal ratio of liver-targeting formulation and ideal extrahepatic accumulation conditions for drugs were obtained. A series of chemically modified gapmers and terminal conjugates of CT102 were constructed. The duration of drug action and stability *in vivo* was significantly improved. $CT102_{MOE5}$ showed superior cell proliferation inhibition and *IGF1R* mRNA-silencing activity. Furthermore, greater drug efficacy at a lower dose and dosing frequency for the specific $CT102_{MOE5}$ conjugate was achieved by enhanced endocytosis via glycosylation. Subsequent transcriptomic and proteomic studies have shown that CT102s can act on the *IGF1R* mRNA and multiple other tumor apoptosis-related pathways.

RESULTS

Optimal screening of formulations based on tissue distribution *in vivo*

Based on previous work,[44] an appropriate molar ratio of carriers (lipid/antisense oligonucleotide [ASO] = 60:1) was preliminarily determined. In this study, the composition ratio of DNCA/CLD was changed to 60:0 (termed DNCA), 40:20 (termed Mix-1), 30:30 (termed Mix), and 20:40 (termed Mix-2) to explore the influence of the formulation ratio on the distribution characteristics *in vivo*. Eight groups were constructed by changing the ratio of DNCA/CLD and incorporating PEG (1%, 6%) (Figure S1). The specific tissue distribution of CT102 was investigated at 4 h, and 1, 4, and 7 days after administration. The five major organs, namely heart, lung, liver, spleen, and kidney, were harvested for fluorescence quantification *in vitro*. The comparison of quantitative fluorescence in each tissue at different time points for each formulation is discussed in detail in section S1 (Figure S2–S4). DSPE-PEG (1%) was the proper addition for balancing accumulation time *in vivo* and liver-targeting characteristics (Figures S5 and S6). One day after administration, the fluorescence quantification of each formulation was analyzed separately. Table 1 shows that different ratios of compositions lead to different distribution patterns *in vivo*. The drug distribution in the liver fluctuated between 30% and 60% under different formulation conditions.

Subsequently, we characterized the basic properties of different formulations with 1% PEG incorporation to investigate their relationship with *in vivo* distribution patterns. First, except for the pure DNCA group, the other formulation groups showed nearly 100% encapsulation efficiency (Figure S7A), suggesting that the variability of the carrier ratio of this delivery system relied on hydrogen bonding, π-π, and electrical interaction forces. With the gradual increase in the proportion of cationic lipids, the surface potential also gradually increased (Figure S7B, DNCA/-8.2 mV, Mix-1/-3.4 mV, Mix/3.9 mV, Mix-2/9.8 mV). Particle size also showed an increasing trend to a certain extent (Figure S7C). The reason for this observation may be that some ASOs attach to the surface of the ON-lipid complexes. With the increase in the proportion of cationic lipids, negatively charged ASOs are more likely to bind with positively charged lipids, thereby promoting an increase in particle size. Therefore, to avoid toxicity problems caused by excessive positive charge while ensuring substantial hepatic accumulation, Mix (DNCA/CLD/PEG/ASO = 30/30/0.6/1) was identified as the optimal formulation and was used for follow-up experiments.

Structural optimization and activity screening of CT102 gapmers

To further improve antitumor efficacy, CT102 was modified with 2′-OMe, 2′-OMOE, and 5-methylcytosine. The specific gapmer modification modes are shown in Table S2. The CCK8 results (Figure 1A) showed that the antitumor activity increased by increasing 2′-ribose modification sites. Among them, $CT102_{MOE5}$ had the greatest efficacy. The 2′-ribose modification greatly increases target affinity and serum stability, thereby enhancing antitumor efficacy. The gene-silencing level of the target mRNA of $CT102_{MOE5}$ was also significantly higher than that of CT102, and approximately 80% gene silencing was achieved (100 nM, Figure 1B). The apoptosis experiment demonstrated (Figures 1C and 1D) that $CT102_{MOE5}$ significantly enhanced the ability to induce late apoptosis, nearly twice that of CT102 (57% vs. 31%). Therefore, $CT102_{MOE5}$ was finally determined to be the optimal candidate, and subsequent molecular conjugation was carried out using $CT102_{MOE5}$.

Construction of $CT102_{MOE5}$ conjugates and formulation characterization

Table S3 lists the structural information of different conjugates of $CT102_{MOE5}$, which are mainly divided into G3 with three GalNAc

Table 1. Fluorescence quantitative analysis (ratio of fluorescence intensity) of different formulations of CT102 in organs 24 h after administration (n = 5)

Organ	ASO (%)	DNCA[a] (%)	Mix-1[a] (%)	Mix[a] (%)	Mix-2[a] (%)	DNCA[b] (%)	Mix-1[b] (%)	Mix[b] (%)	Mix-2[b] (%)
Heart	3.0	0.8	1.8	3.0	2.4	1.9	5.2	1.8	5.4
Lung	3.6	0.1	2.3	3.8	1.3	1.9	5.7	1.8	4.0
Liver	4.6	18.4	45.2	64.5	57.8	2.4	30.2	32.2	40.6
Spleen	0.5	7.2	24.4	15.7	27.3	1.0	4.6	4.7	11.0
Kidney	88.3	73.5	26.4	13.0	11.2	92.8	54.4	59.5	39.0

DNCA, Mix, Mix-1, and Mix-2 represent DNCA:CLD molar ratios of 60:0, 40:20, 30:30, and 20:40, respectively.
[a]Represents 1% DSPE-PEG incorporation in formulations of ASOs.
[b]Represents 6% DSPE-PEG incorporation in formulations of ASOs.

molecular clusters and monosaccharide structures with different types of sugars, such as acetylgalactosamine (Gal), acetylglucosamine (Glu), and mannose (Man). Due to the length and connection method of the linker, the conjugates were subdivided into sG, Gal(N/O), Glu(N/O), and Man(N/O). Among them, N represents the connection mode of the amide bond, and O represents the connection mode of the ether bond.

Due to the similar structures of various conjugates, some representative candidates were selected for submicroscopic characterization, zeta potential analysis, and particle size investigation (Figure S8). The particle size of each conjugate was greater than that of $CT102_{MOE5}$, among which G3-$CT102_{MOE5}$ had the largest particle size, reaching 143 nm, indicating that the molecular weight of each conjugate has a direct influence on the particle size. The metabolic stability of each representative conjugate was also investigated (Figure S9). In general, the original sequence CT102 has relatively excellent enzyme resistance and serum stability due to the phosphorothioate modification, and was not completely degraded in serum for 8 days. Moreover, the stability of $CT102_{MOE5}$ is more prominent, and the degradation proportion at all time points in the experiment is very small. The gapmer already possessed strong serum stability, and the conjugates did not significantly increase serum stability.

Effect of chemical modification and conjugation on distribution *in vivo*

The distribution and accumulation time of CT102, its representative gapmer $CT102_{MOE5}$, and conjugate G3-$CT102_{MOE5}$ *in vivo* were further compared. Both CT102 and $CT102_{MOE5}$ showed excellent liver accumulation ability by intravenous administration. From the *in vivo* imaging and quantitative fluorescence analysis, the gapmer $CT102_{MOE5}$ significantly enhanced the *in vivo* stability. The fluorescence signal lasted more than 30 days after a single dose, while the unmodified CT102 was only about 3 weeks (Figure S10). The conjugate G3-$CT102_{MOE5}$ should theoretically further prolong the half-life of ASOs, but quantitative fluorescence analysis showed that the difference is not apparent (Figure 2A). It was observed that the fluorescent signal of $CT102_{MOE5}$ and G3-$CT102_{MOE5}$ can reach 40 days after a single dose in the investigation of the longest residence time *in vivo*. The reason should be that both phosphorothioate and gapmer modification significantly increased the enzyme resistance of the ASO and prolonged its half-life, so the gain of the conjugation on stability is not outstanding. Moreover, the imaging results of the first 3 days showed that G3-$CT102_{MOE5}$ presented better liver accumulation ability than that of $CT102_{MOE5}$ (Figure 2A).

Further fluorescence quantification of G3-$CT102_{MOE5}$ and $CT102_{MOE5}$ in the main organs was carried out. The fluorescence signal of G3-$CT102_{MOE5}$ was stable and continuous in the liver (Figure 2B), and it still exhibited noticeable liver accumulation after up to 15 days, making it an ideal liver-targeting agent. Compared with $CT102_{MOE5}$ (Figures 2C and 2D), the proportion of fluorescence intensity of G3-$CT102_{MOE5}$ increased by ~10% in the liver at the same time point. Therefore, these results suggest that $GalNAc_3$ conjugation and lipid delivery have a synergistic effect, and combining the two can further improve the liver-targeting ability. In conclusion, G3-$CT102_{MOE5}$ has the optimal liver-targeting ability and is worthy of further efficacy experiments.

Comparison of the transmembrane ability of modified CT102s

Subsequently, the differences in the transmembrane ability of modified CT102s in HepG2 and Huh7 cells were compared using flow cytometry 6 h after administration. The drug uptake rates in HepG2 cells were CT102 (62.5%), $CT102_{MOE5}$ (67.3%), G3-$CT102_{MOE5}$ (70.1%), and Glu-$CT102_{MOE5}$ (74.2%) (Figures 3A and S11). In Huh7 cells, drug uptake rates were CT102 (86.4%), $CT102_{MOE5}$ (87.8%), G3-$CT102_{MOE5}$ (89.5%), and Glu-$CT102_{MOE5}$ (91.6%) (Figures 3B and S11). Therefore, both G3 and Glu conjugates improved the uptake of drugs to a certain extent, which may be a result of glycosylated receptors on the cell surface. Moreover, tumors exhibit enhanced sugar uptake properties to maintain their rapid cell proliferation, which is beneficial for increasing tumor cell-specific endocytosis of drugs and improved uptake rates were more evident in HepG2 cells.

The specific intracellular localization of each modified CT102 was investigated by confocal microscopy. Every modified CT102 entered the cells and a high proportion of nuclear colocalization was observed 6 h after administration (Figure 3D). Interestingly, we found that the proportion of conjugate G3-$CT102_{MOE5}$ in the nucleus was significantly reduced. Through analysis of the ASO fluorescence intensity in the nucleus and cytoplasm (Figure 3C), it was observed that the transnucleus capability of G3-$CT102_{MOE5}$ was inferior to that of $CT102_{MOE5}$ and Glu-$CT102_{MOE5}$ ($p < 0.01$). This result suggested

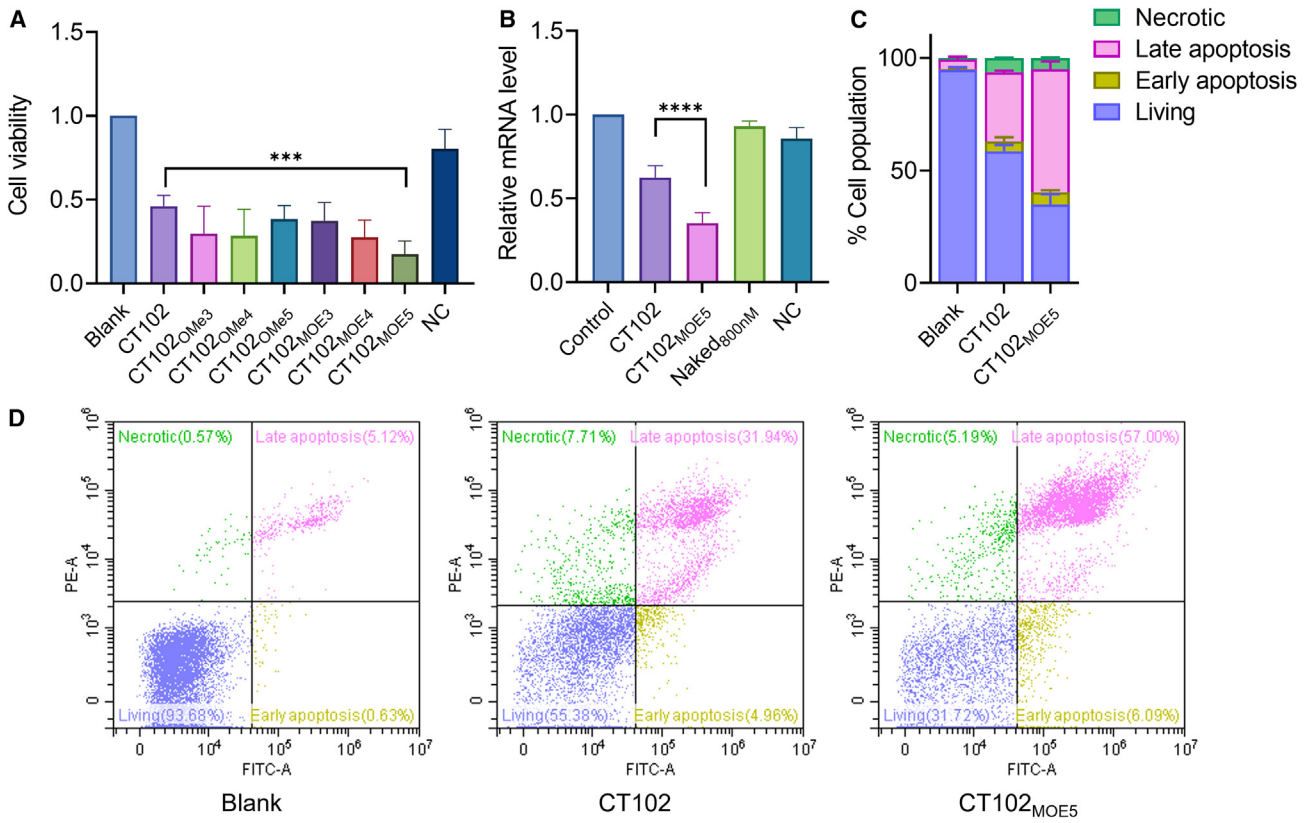

Figure 1. Antitumor activities of CT102 gapmers/Mix in HepG2 cells

(A) The proliferation inhibitory activity of each gapmer/Mix. (B) The silencing activity of CT102 and $CT102_{MOE5}$ nanoparticles on target *IGF1R* mRNA. (C) The ability of CT102 and $CT102_{MOE5}$ nanoparticles to induce cell apoptosis. (D) Flow cytometry analysis of the cell cycle influenced by CT102 and $CT102_{MOE5}$ nanoparticles. ASO, 100 nM, n = 3; ***p < 0.001, ****p < 0.0001; data are represented as mean ± SD.

that, although the conjugation structures may improve cellular uptake to a certain extent, the size of a conjugated structure affects the ability of an ASO to enter the nucleus. The distribution of an ASO in the nucleus is an essential part of its overall activity. Therefore, the inconsistency between the intracellular uptake and intranuclear distribution of the conjugated structures, especially G3-$CT102_{MOE5}$, and their activities deserve further confirmation *in vitro* and *in vivo*.

The antiproliferative ability and gene silencing of $CT102_{MOE5}$ conjugates

The difference in activity of each conjugate was compared by examining the cell proliferation inhibition and target mRNA-silencing ability. According to the results, the conjugates did not affect the antisense activity, and several had slightly increased activity (Figures 3E and 3F). In terms of target gene-silencing activity, there was no significant difference between the conjugate groups, and the activities of Gal-$CT102_{MOE5}$, Glu-$CT102_{MOE5}$, and Man-$CT102_{MOE5}$ were slightly increased. The CCK8 results showed that the conjugates generally had higher cell proliferation inhibition on HepG2 cells, which was consistent with the higher cellular uptake rate found in HepG2 than Huh7 cells in the flow cytometry experiment. In addition, a longer linker length in the monosaccharide conjugates produced inferior effects. Long-chain conjugates (Gal(N/O), Glu(N/O), and Man(N/O)) had decreased inhibitory activity against cell proliferation compared with that of short-chain conjugates (Gal, Glu, and Man). Based on the above results, Gal-$CT102_{MOE5}$, Glu-$CT102_{MOE5}$, Man-$CT102_{MOE5}$, and G3-$CT102_{MOE5}$ were determined to be the optimal structures for subsequent *in vivo* efficacy experiments.

Antitumor efficacy *in vivo*

Tumor development after administration of different formulations was monitored every 7 days by a small animal *in vivo* imager (Figure S12). The tumor bioluminescence growth results of the drug efficacy in mice for 28 days (Table 2; Figures 4A and 4B) showed that, compared with sorafenib and CT102, $CT102_{MOE5}$ and several other conjugates had significantly different antitumor efficacy, indicating that $CT102_{MOE5}$ could enhance tumor growth inhibitory activity through 2′-OMOE gapmer modification. Moreover, the conjugate groups (G3/Gal/Glu/Man-$CT102_{MOE5}$) were superior to the $CT102_{MOE5}$ group, and the average tumor size on day 28 was 15.0, 9.4, 7.5, and 18.2 times that of day 0 ($CT102_{MOE5}$, 24.6 times). Glu-$CT102_{MOE5}$ had the most robust tumor inhibitory effect among all drug groups, and the tumor growth fold change within 1 week after drug withdrawal was the smallest, only 1.1 times.

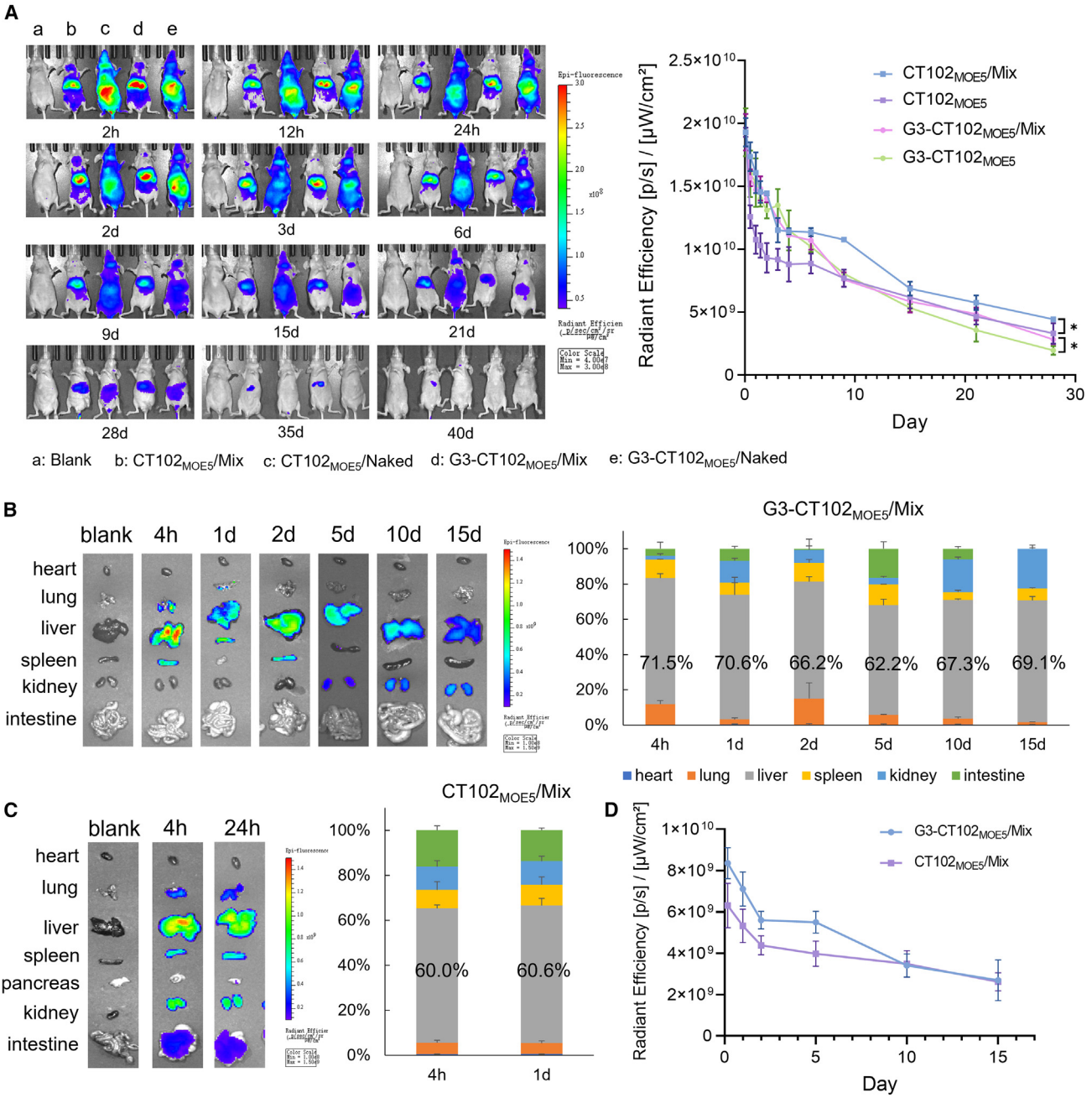

Figure 2. Biodistribution of $CT102_{MOE5}$ and G3-$CT102_{MOE5}$ encapsulated with Mix

(A) Biodistribution and quantitative fluorescence analysis of $CT102_{MOE5}$ and G3-$CT102_{MOE5}$ in BALB/c nude mice treated with GenOpti (blank, a), $CT102_{MOE5}$/Mix (b), $CT102_{MOE5}$ (c), G3-$CT102_{MOE5}$/Mix (d), and G3-$CT102_{MOE5}$ (e) by tail intravenous injection. Images were taken at 2, 12, and 24 h and at 2, 3, 6, 9, 15, 21, 28, 35, and 40 days by an *in vivo* imaging system. (B) Quantitative fluorescence analysis of G3-$CT102_{MOE5}$/Mix in tissues. (C) Quantitative fluorescence analysis of $CT102_{MOE5}$/Mix in tissues. (D) Quantitative fluorescence analysis of G3-$CT102_{MOE5}$/Mix and $CT102_{MOE5}$/Mix in the liver. Mix: DNCA/CLD/PEG/ASO = 30/30/0.6/1, n = 3, *p < 0.05, data are represented as mean ± SD.

Afterward, quantitative evaluation of intratumoral target gene knockdown and immunofluorescence analysis of IGF1R protein were performed. The results showed that the silencing of the target gene *IGF1R* (Figure 4C) was consistent with the changes in protein expression (Figures 4D and 4E). The gapmer $CT102_{MOE5}$ further enhanced the *in vivo* activity of CT102, effectively silencing *IGF1R* mRNA expression levels ($p < 0.001$), and reducing subsequent protein expression ($p < 0.01$). Compared with $CT102_{MOE5}$, G3-$CT102_{MOE5}$

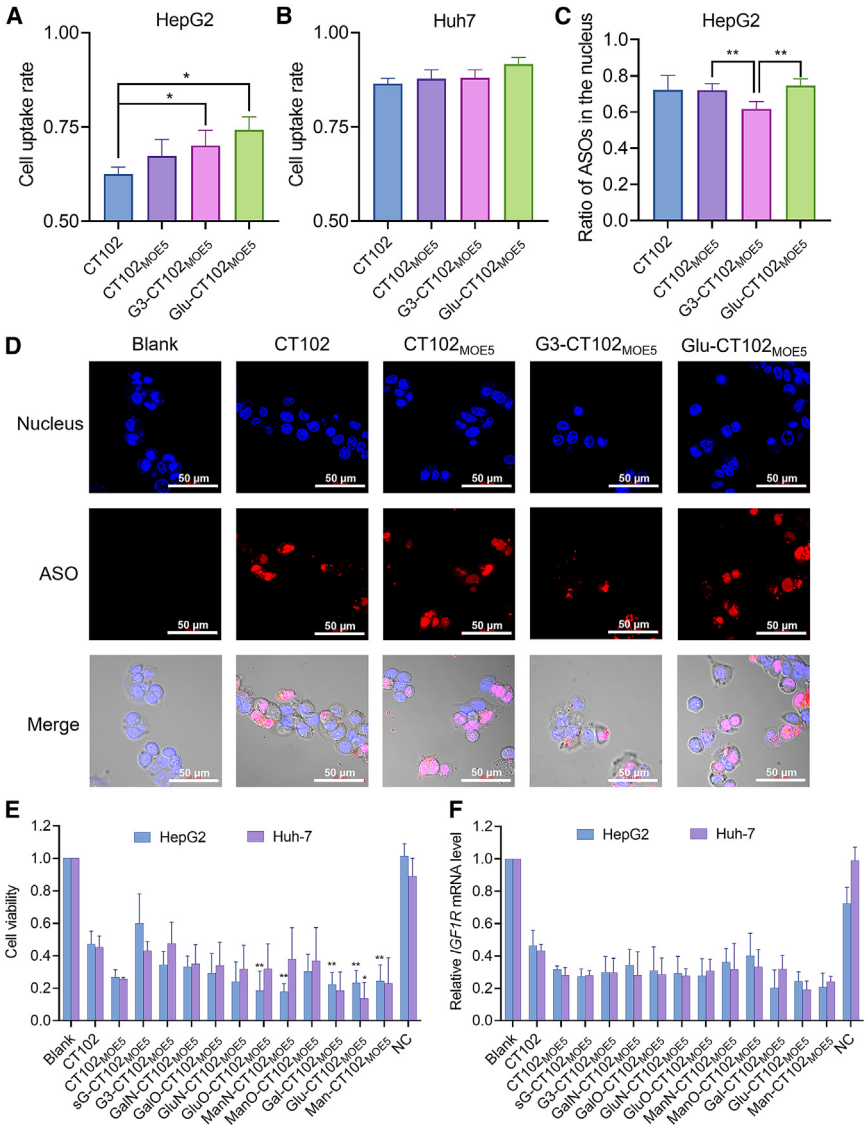

Figure 3. Activity evaluation of modified CT102s/Mix *in vitro*

(A and B) Flow cytometry analysis of the cellular uptake of modified CT102s in HepG2/Huh7 cells (100 nM, 6 h, n = 3). (C) The proportion of modified CT102s colocalized with nucleus in HepG2 cells (n = 5). (D) Confocal imaging of intracellular localization of modified CT102s in HepG2 cells (red represents ASOs, blue represents nucleus). Scale bar, 50 μm. (E and F) The proliferation inhibitory activity and silencing activity on the target *IGF1R* mRNA of each $CT102_{MOE5}$ conjugate in HepG2 and Huh7 cells (100 nM, n = 5, p value was compared with CT102). *$p < 0.05$, **$p < 0.01$; data are represented as mean ± SD.

showed no advantage at the gene and protein levels. However, compared with $CT102_{MOE5}$ and G3-$CT102_{MOE5}$, Glu-$CT102_{MOE5}$ further enhanced gene silencing and inhibited protein expression levels ($p < 0.05$). Overall, the activity data results showed that Glu-$CT102_{MOE5}$ significantly inhibited tumor growth and was determined to be the optimal active structure to combat HCC cells.

In vivo safety verification

To investigate the safety of DCP-encapsulated ASO formulations *in vivo*, changes in mouse body weight, biochemical blood indexes, and pathological sections were measured. Throughout the experimental period, there was no significant difference in the body weight of the mice (Figure S13B), indicating that each ASO formulation was well tolerated. In addition, the blood samples collected at the end of the experiment showed that the levels of aspartate aminotransferase (AST), alanine aminotransferase (ALT), total bilirubin (TBIL), urea nitrogen (BUN), and creatinine (CREA), which are biochemical blood indexes of liver and kidney function, were all within the normal range in each group (Figure S13A). Hematoxylin and eosin (H&E)-stained paraffin sections showed (Figure S13C) prominent tumor infiltration in the saline group. Liver injury was more severe in the saline group than in the other groups, so normal liver tissue could not be harvested. However, the liver tissues of the ASO groups were relatively normal, and no severe damage was found. In conclusion, the *in vivo* safety of each formulation was effectively verified.

Functional mechanisms of modified CT102s

The functional mechanisms by which the modified CT102s caused biological changes were studied. The protein expression levels of IGF1R, AKT, p-AKT, PI3K, and p-PI3K were investigated by western blotting. After the administration of CT102, $CT102_{MOE5}$, and Glu-$CT102_{MOE5}$ for 24 h, the IGF1R protein level was significantly decreased, and both the gapmer $CT102_{MOE5}$ and the conjugate Glu-$CT102_{MOE5}$ efficiently inhibited the phosphorylation levels of PI3K and AKT, among which Glu-$CT102_{MOE5}$ showed the most significant inhibition ability (Figure 5A).

Moreover, the cell proliferation inhibition and gene-silencing activities of ASOs (CT102, N-04, N-06) and siRNAs (si*IGF1R*-1, si*IGF1R*-2) targeting *IGF1R* mRNA were compared (Figure 5D). Among them, the target mRNA site of ASO N-04 is separated from that of CT102 by 52 bases, which is near the end of exon 1. ASO N-06 targets the second exon of *IGF1R* mRNA, which partially overlaps with the si*IGF1R*-1 targeting site. The targeting site of si*IGF1R*-2 is the same as that of CT102. At the same concentration (50 nM), the *IGF1R* mRNA-silencing activity of ASOs and siRNAs in HepG2 cells

Table 2. Protocol for the administration of ASO formulations

Group	Mice	Name	Dose	Administration	Frequency
1	5–6/group	saline (blank)	100 μL	i.v.	every 4 days, 6 times in total (day 0, 4, 8, 12, 16, 20)
2		CT102/DCP	2 mpk		
3		$CT102_{MOE5}$/DCP			
4		G3-$T102_{MOE5}$/DCP			
5		Gal-$CT102_{MOE5}$/DCP			
6		Glu-$CT102_{MOE5}$/DCP			
7		Man-$CT102_{MOE5}$/DCP			
8		sorafenib (positive control)	20 mpk	i.g.	every day, 20 times in total

was comparable (Figure 5B), and there was no significant difference (~60%). The results of cell proliferation inhibitory activity showed (Figure 5C) that CT102 (70.9%) had significantly stronger inhibitory activity on HepG2 cell proliferation than that of N-04 (48.5%), N-06 (42.5%), si*IGF1R*-1 (21.3%), and si*IGF1R*-2 (22.6%). These results indicated that CT102 exhibits antitumor activity in a complicated manner and suggested that CT102 not only inhibits *IGF1R* expression but also might act on other apoptosis-related genes.

Transcriptomics and proteomics analysis of modified CT102s

Thus, transcriptomic and proteomic analyses were carried out to evaluate possible targets of modified CT102s *in vitro*. The results showed thousands of altered mRNAs and proteins, and many signaling pathways were modified (Figures 6B and S14). Compared with the empty lipids (Mix), CT102 had 13 genes and proteins upregulated and 5 genes and proteins downregulated at the same time (Figure 6A). The differentially expressed genes were enriched in a variety of tumor-related signaling pathway protein genes. In addition to the known changes in tyrosine kinase receptor-mediated signal transduction via IGF1R, there are also significant differences in PPAR, P53, DNA replication, mismatch repair, and other signaling pathways (Figures 6C–6E). Besides, through rational chemical modification, the results showed that the number of genes and proteins affected by the gamper $CT102_{MOE5}$ and conjugate Glu-$CT102_{MOE5}$ decreased, which enhanced the "on-target" effect of CT102 to some extent. The proteomic results showed that approximately 25% of the differentially expressed proteins in the CT102, $CT102_{MOE5}$, and Glu-$CT102_{MOE5}$ groups were localized in the nucleus (Figure S15), including functional proteins involved in transcription, phosphorylation, phosphatase activation, and DNA/RNA binding proteins. It was found that modified CT102s could decrease *IGF1R* mRNA expression levels in both the nucleus and cytoplasm (Figure 6F) and had a significant effect on the expression of *GAS2* (GenBank: NM_001143830), *POLA2* (GenBank: NM_002689), *LGALS2* (GenBank: NM_006498), and *IGFBP1* (GenBank: NM_000596), which have functional roles in the occurrence and development of tumors, possibly by imperfect base pairing (Figure 6G; Table S4). In addition, Glu-$CT102_{MOE5}$ also inhibited the phosphatidylinositol signaling, necroptosis, and Wnt signaling pathways. Genes related to pantothenic acid and CoA biosynthesis were also remarkably downregulated (Figure S16).

DISCUSSION

ASOs hold great therapeutic promise for the treatment of nervous system diseases, muscle diseases, cardiovascular and metabolic diseases, eye diseases, and cancer as a result of their precise targeting and relatively easy preparation.[45–47] However, their effective delivery *in vivo* remains a major obstacle. Unfortunately, since the first LNP-delivered siRNA was introduced into the pharmaceutical market in 2018, no LNP-delivered ON drug has entered phase III clinical trials, indicating the limitations of existing lipid delivery technologies based on electrostatic interactions. In this study, we used DCP, a lipid delivery system based on hydrogen bonding, π-π stacking, and electrostatic interactions, to achieve efficient transfection of the ASO CT102 into HCC cell lines.

Studies have shown that delivery of ASOs by liposomes may not be well correlated *in vivo* and *in vitro*.[48] Therefore, we screened and optimized formulations based on *in vivo* distribution rather than *in vitro* activity. An excellent liver-targeting formulation (DCP) was obtained through systematic quantitative fluorescence investigation of different organs. Herein, it seems that there is a linear relationship between the proportion of lipid components, surface charge, particle size, and distribution pattern *in vivo*. Differences in the proportion of lipids directly affect the surface electrical properties, which may significantly affect the formation and properties of surface protein crowns during its transportation *in vivo*,[49,50] thus affecting the interaction of liposomes with tissues and cell surfaces. The ONs encapsulated in DNCA only have a high negative charge and obvious extrahepatic distribution (Table 1; Figure S1). However, a surface charge that is too negative will affect cellular uptake and may cause a decrease in encapsulation efficiency. The ASOs tended to be distributed in the liver when the surface electricity of the formulation was greater than 0 mV. However, toxicity caused by a high positive charge should also be considered. A formulation with a surface potential between −8 and 0 mV (Mix-1) has optimal encapsulation efficiency but low accumulation in the liver, which is not suitable for the treatment of HCC. Eventually, Mix (DNCA/CLD/PEG/ASO = 30/30/0.6/1, 1% PEG, molar ratio, surface potential 3.9 mV) was determined as the final formulation ratio based on various factors.

Next, the structural optimization and delivery study of ASO CT102 in the treatment of HCC were carried out. *In vitro* experiments showed

A

Group		DAY21/ DAY0	DAY28/ DAY0	DAY28/ DAY21
1	Saline	52.5	74.3	1.4
2	CT102	22.8	38.2	1.6
3	$CT102_{MOE5}$	12.5	24.6	1.9
4	$G3\text{-}CT102_{MOE5}$	9.3	15.0	1.6
5	$Gal\text{-}CT102_{MOE5}$	4.5	9.4	2.0
6	$Glu\text{-}CT102_{MOE5}$	6.7	7.5	1.1
7	$Man\text{-}CT102_{MOE5}$	9.7	18.2	1.8
8	Sorafenib	13.7	36.4	2.6

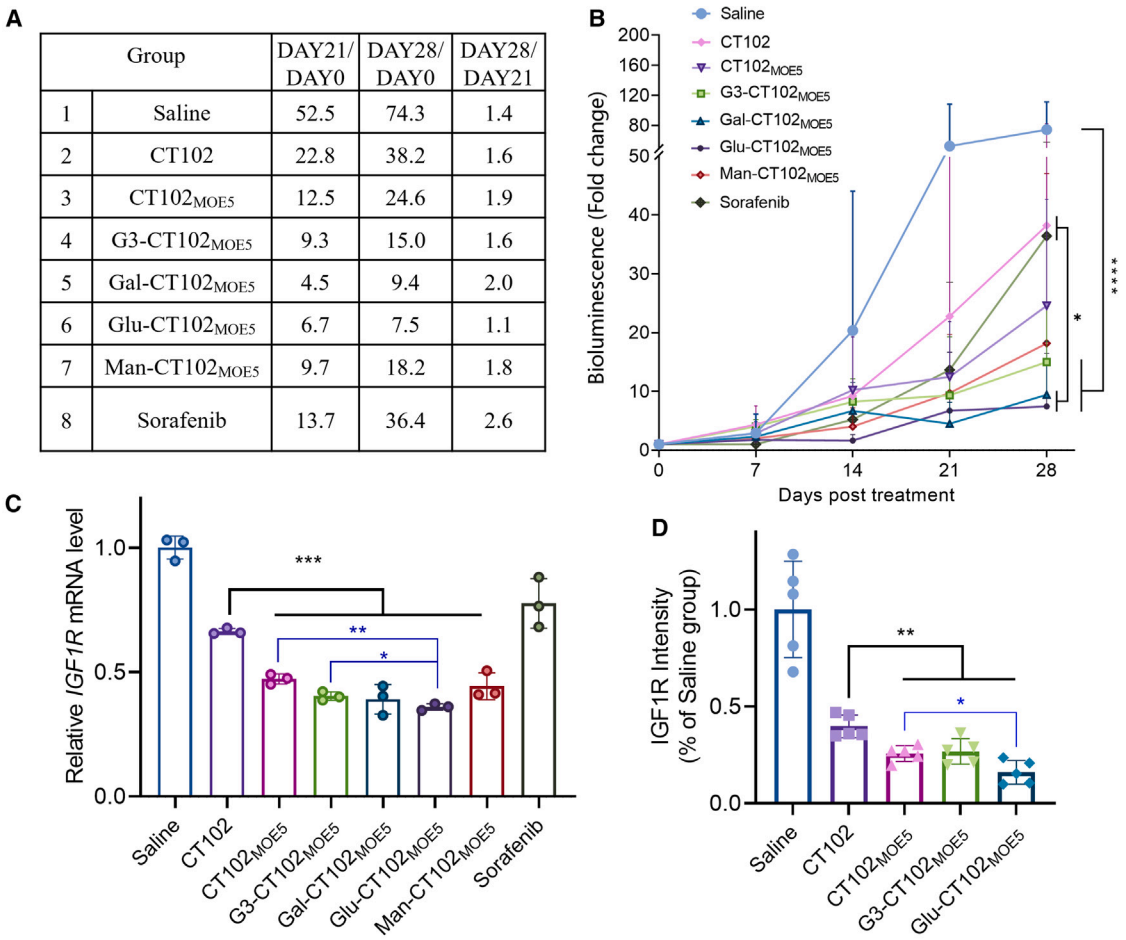

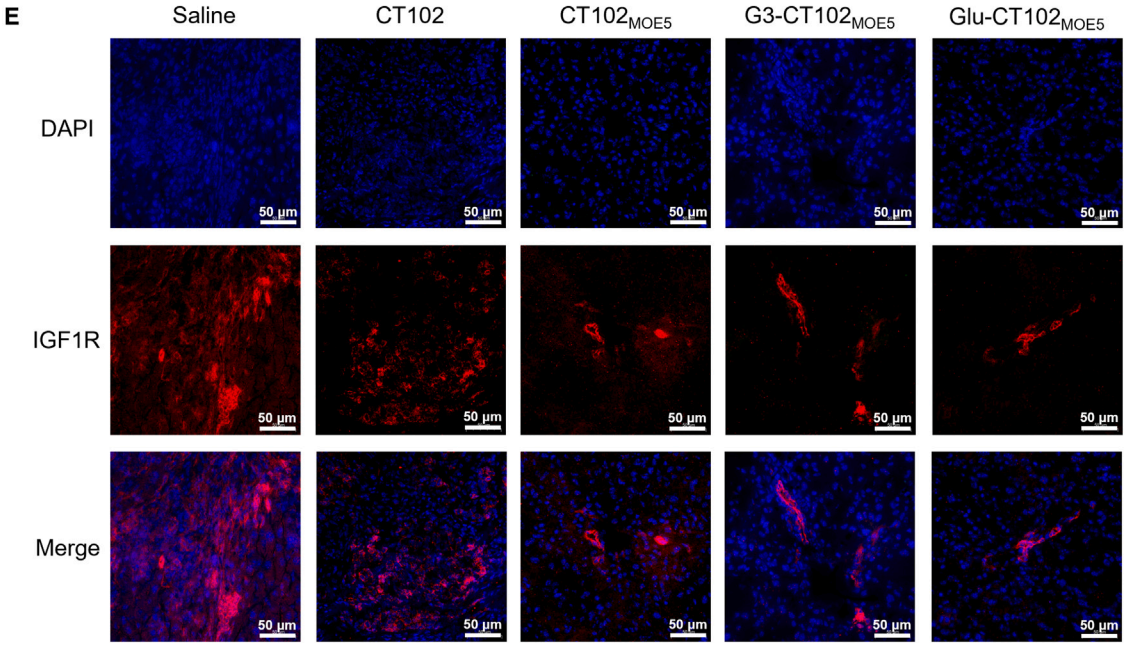

(legend on next page)

that the activity of gapmer CT102 was significantly improved when it was modified with 2'-OMOE. The silencing level of target genes reached nearly 80% (100 nM), which could be related to increased target affinity (Figure 1). On this basis, some glycoconjugates further promoted cell proliferation inhibition and target gene silencing, which might be accomplished through enhanced cellular uptake by glycosyl receptors on the cell surface (Figures 3A and 3B). In terms of *in vivo* efficacy, modified CT102s reduced the dose and dosing interval (2 mpk/4 days) by DCP delivery due to excellent serum stability. Moreover, the tumor inhibitory effect of the conjugate was also improved, and Glu-CT102$_{MOE5}$ showed the best antitumor proliferation effect (Figure 4).

It is worth mentioning that the GalNAc$_3$ conjugation strategy is rarely used to treat HCC because ASGPRs are expressed at low levels on the surface of HCC cells. However, there is also a view that the receptor is highly abundant on the surface of liver cells. Even if the ASGPR expression is low, the remaining receptor amount is sufficient to mediate drug entry into the cell.[51,52] Therefore, Ionis Pharmaceuticals generated a GalNAc$_3$-ASO for the treatment of HCC. However, subsequent *in vivo* verification showed that the conjugate did not show a significant difference compared with the nonconjugate, which was also attributed to the above-mentioned low ASGPR expression.[53] Herein, we also constructed a GalNAc$_3$-ASO, G3-CT102$_{MOE5}$, and obtained similar activity results through intravenous liposomal administration instead of subcutaneous administration. We found that the biological distribution of ASO in the nucleus played a pivotal role in its overall activity. Through the confocal colocalization experiment (Figures 3C and 3D), we believe that another major reason for the decreased activity of G3-CT102$_{MOE5}$ is the influence of the large conjugation group on its nuclear entry ability. The above results provide guidance for the structural design of ASO conjugates in the future. In addition to the targeting significance of the conjugate group, the size of the group and the length of the linker also need to be carefully considered. A conjugated moiety that is too large and a linker that is too long may be ineffective.

The PI3K-AKT signaling pathway is abnormally activated in many cancer types, plays a central role in tumor cell proliferation and survival,[54] and is necessary for regulating cell proliferation, differentiation, and apoptosis. Analysis of protein expression showed that CT102 and its derivative conjugates (especially Glu-CT102$_{MOE5}$) could effectively reduce the synthesis of the target protein IGF1R to varying degrees, thereby inhibiting the downstream PI3K-AKT signaling pathway and subsequently suppressing tumor growth (Figure 5A). Interestingly, we found that ASOs and siRNAs targeting *IGF1R* mRNA showed significant differences in their antiproliferation abilities, while their target gene-silencing ability was similar, suggesting that ASOs may have more functional roles in cells than siRNAs have (Figures 5B and 5C). Although both antisense and RNAi are effective RNA-silencing technologies, ASOs act on more signaling pathways and cycles through multiple mechanisms, thus showing better efficacy in inhibiting tumor development.

Therefore, the potential mechanisms, especially the specific roles of such a large proportion of modified CT102s in the nucleus, are worth exploring. Combined with the results of transcriptomic and proteomic analysis, modified CT102s not only play a role in the PI3K-AKT pathway activated by tyrosine kinase but also function in DNA replication, anti-inflammation, the immune microenvironment, and many other processes affecting tumor growth (Figure 6). Also, they could interact with other mRNAs via imperfect matches (such as *GAS2*, *POLA2*, and *LGALS2*), thereby downregulating the expression of the related proteins and jointly inducing the apoptotic process of tumor cells (Table S4). These results demonstrated that ASOs cannot only bind to mature mRNA to hinder translation and exert silencing activity. There are many possibilities for their role in the nucleus, such as binding to the pre-mRNA, initiating the cleavage mechanism, and blocking the processing of the pre-mRNA to form mature mRNA. They may also combine with complementary double-stranded DNA in the nucleus to form a triplex,[55] suppress the transcription of DNA, or bind to transcription factors or transcription complexes through the aptamer mechanism to effectively influence their transcription,[56–58] resulting in the upregulation of related genes or proteins indirectly, such as *IGFBP1*.

In conclusion, this study offers a promising ASO formulation possessing longer-lasting anti-HCC efficacy and reveals the function and mechanism of modified ASOs delivered by DCP lipids, which exhibit excellent potential for further clinical application.

MATERIALS AND METHODS

ASO synthesis, cell culture, and preparation of ASO liposome nanocomplexes

All ASO samples were synthesized by an ABI-394 DNA synthesizer in the laboratory. Specific sequences, modification information, and synthesis methods are described in the supplemental information. The human HCC cell lines HepG2 and Huh7 (Procell Life Science & Technology, Wuhan, China) were cultured in DMEM (Zhongke Maichen Technology, Beijing, China) supplemented with 10% fetal bovine serum (FBS, Gibco, Grand Island, NY) in a 5% CO_2 incubator at 37°C. The ASO liposome nanocomplexes were constructed as described previously.[44]

Figure 4. Antitumor efficacy of modified CT102s/Mix formulations on orthotopic HCC model mice

(A) Bioluminescence comparison of tumors treated with ASOs/Mix at different time points. (B) Bioluminescence growth rate of different groups (n = 5–6). (C) Quantitative analysis of *IGF1R* mRNA expression level in tumor tissue of each treatment group (n = 3). (D) Percentage of fluorescence intensity of IGF1R protein of each treatment group compared with the saline group (n = 5). (E) Immunofluorescence assays were used to evaluate the protein expression of IGF1R in tumor tissues of each treatment group; red represents the protein expression of IGF1R, and blue represents the nucleus. Scale bar, 50 μm. *p < 0.05, **p < 0.01, ***p < 0.001; data are represented as mean ± SD.

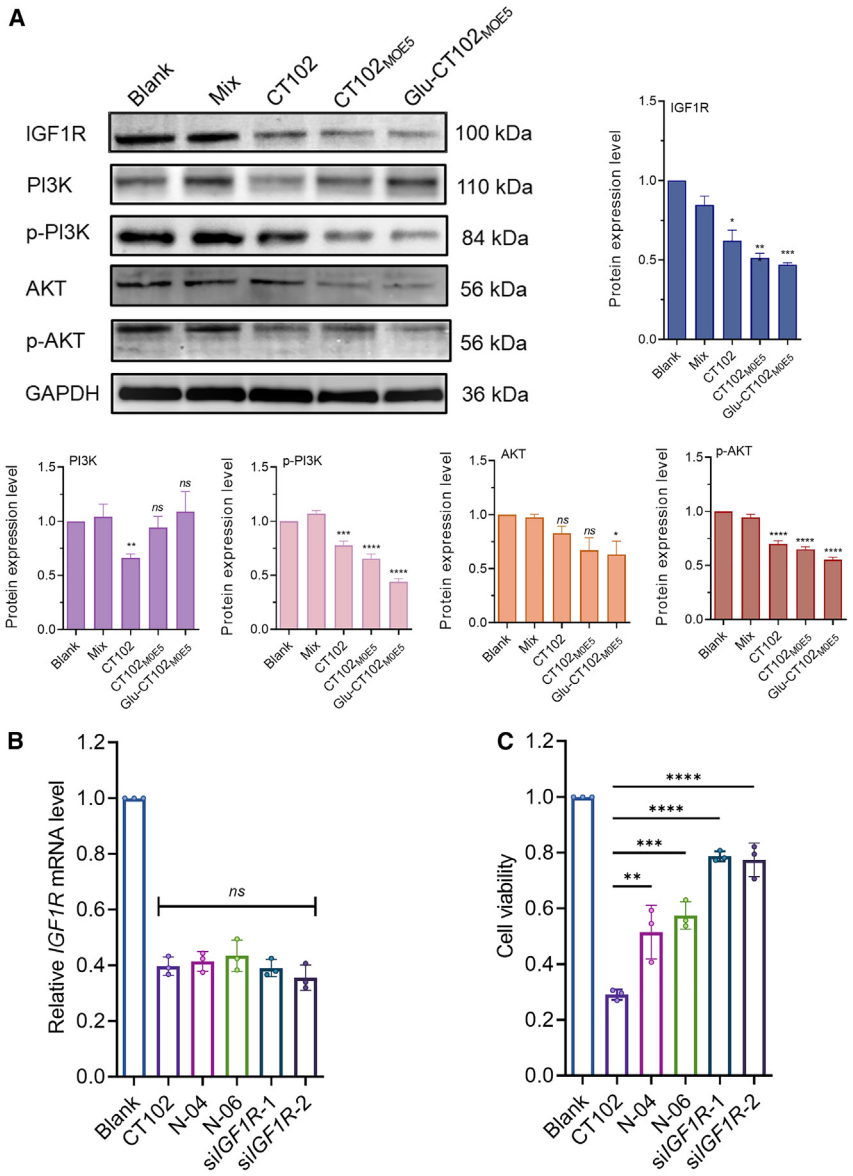

D

Name	Sequence (5'-3')	mRNA site	Exon number
CT102	TCCTCCGGAGCCAGACTTCA	5052-5071	Exon 1
N-04	TTCTCCACTCGTCGGCCAGA	5124-5143	Exon 1
N-06	GCTGCTGATAGTCGTTGCGG	63053-63072	Exon 2
si*GF1R*-1	SS: CGACUAUCAGCAGCUGAAGTT AS: CUUCAGCUGCUGAUAGUCGTT	63059-63077	Exon 2
si*GF1R*-2	SS: GAAGUCUGGCUCCGGAGGATT AS: UCCUCCGGAGCCAGACUUCTT	5053-5071	Exon 1

Figure 5. Functional mechanisms of modified CT102s

(A) Protein expression of IGF1R and PI3K-AKT pathway-related proteins (n = 3, p value was compared with Mix). (B) Gene-silencing activity of ASOs and siRNA targeting *IGF1R* mRNA in HepG2 cells (50 nM, 24 h, n = 3). (C) Proliferation inhibitory activity of ASOs and siRNAs targeting *IGF1R* mRNA in HepG2 cells (50 nM, 48 h, n = 3). (D) The sequence information of ASOs and siRNAs targeting different regions of *IGF1R* mRNA. ns $p > 0.05$, *$p < 0.05$, **$p < 0.01$, ***$p < 0.001$, ****$p < 0.0001$; data are represented as mean ± SD.

The construction of different ASO conjugates

The synthesis of all conjugate precursors and confirmed data are described in detail in the supplemental information (Figures S17–S51). All conjugates were constructed by reactive ester reactions or phosphoramidite methods, followed by a standard DNA purification protocol, and target samples (Table S5) were obtained with high purity.

Particle sizes and zeta potentials test

The ASO nanocomplexes (ASO: 1 μM) were diluted in 1× PBS (Zhongke Maichen Technology) solution (0.4 mL), and filtration by 200 nm LiposoFast-Basic LF-1 (Avestin) was performed before measurement. The sizes and zeta potentials were measured using a Zetasizer Nano ZSP instrument (Malvern Instruments) with photon correlation spectroscopy at a scattering angle of 90°, 20°C. Data were analyzed using an ELS-8000 software package.

TEM analysis

The ASO nanocomplexes (ASO: 5 nmol) were dissolved in PBS (100 μL). Then the nanoparticles were visualized using the uranyl acetate-negative staining method. The sample was dripped onto the PARA film and covered with a copper mesh transparent film. The film was removed after 1–2 min and the liquid was removed from the edges with absorbent paper. Afterward, the copper mesh was stained with 1% uranyl acetate for 1 min and observed through a JEM-1400 Plus transmission electron microscope (JEOL, Japan).

Serum stability assay

Unformulated ASOs (10 pmol/well) were incubated in 1× PBS at 37°C containing 50% FBS. The samples were collected at the indicated time points and frozen in an ultralow temperature freezer at −80°C. Subsequently, 2 μL 6× DNA loading buffer (DingGuo, Beijing, China) was added to each sample, followed by vortexing. Then, all samples were electrophoresed on 20% polyacrylamide gels at 110 V for 120 min. The gels were visualized by 5 μL/gel 10,000× SYBR Gold (Life, Invitrogen,

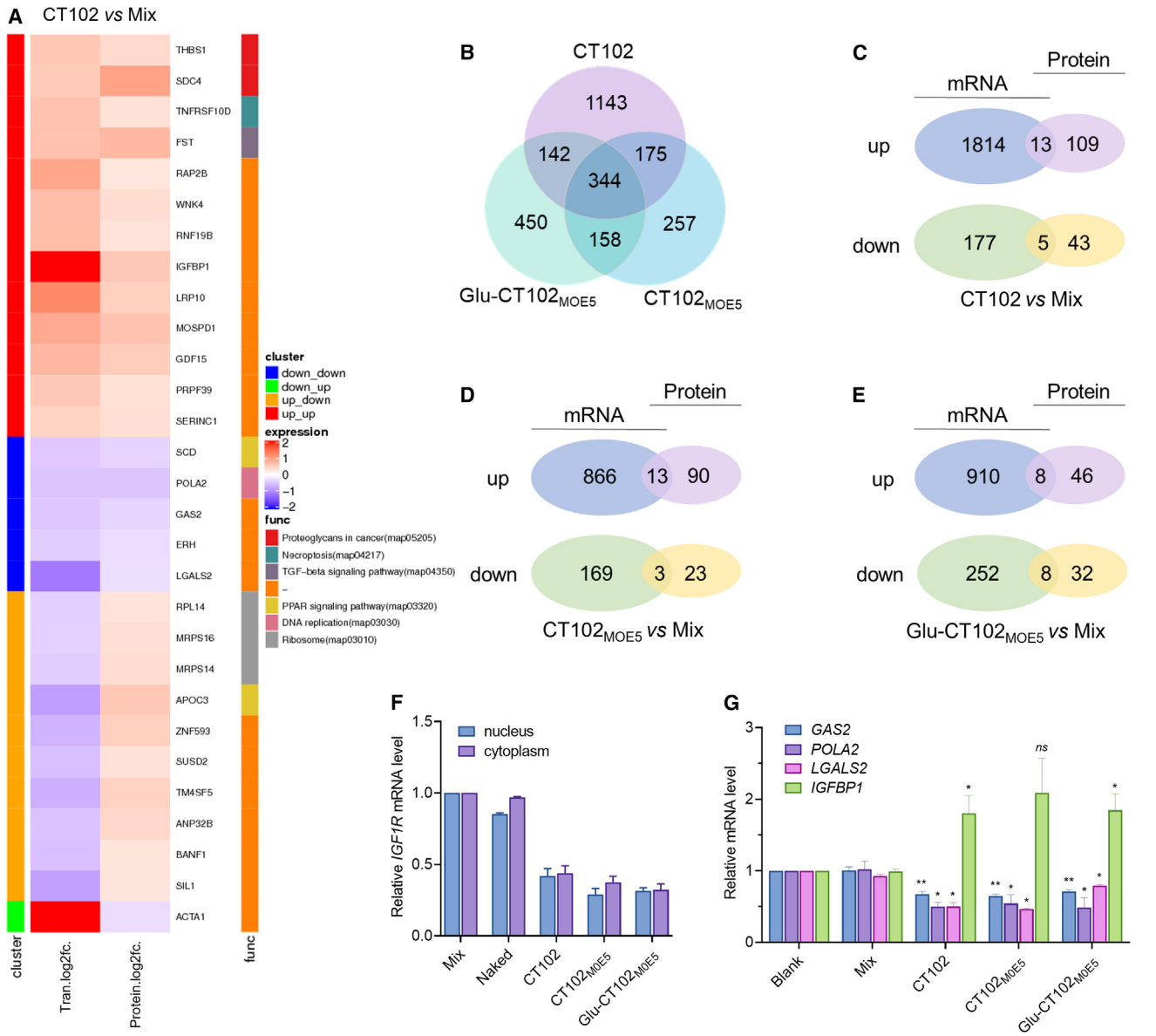

Figure 6. Potential targets of modified CT102s/Mix

(A) The KEGG enrichment analysis results classified the functional genes and proteins that were differentially expressed between the CT102/Mix and Mix group. The p values were less than 0.05 and the fold changes were more than 2 for gene expression analysis and 1.2 in protein expression analysis. (B) The number of genes regulated by CT102/Mix, $CT102_{MOE5}$/Mix, and Glu-$CT102_{MOE5}$/Mix in comparison with the Mix group. (C–E) The number of genes and proteins regulated by CT102/Mix or $CT102_{MOE5}$/Mix or Glu-$CT102_{MOE5}$/Mix in comparison with the Mix group. (B–E) The p values were less than 0.05, and fold changes (FC) were more than 2. (F) Silencing efficiency of intranuclear and cytoplasmic *IGF1R* mRNA (50 nM, n = 3). (G) Quantitative analysis of *GAS2*, *POLA2*, *LGALS2*, and *IGFBP1* mRNA expression levels by qPCR assay (50 nM, n = 3; ns $p > 0.05$, *$p < 0.05$, **$p < 0.01$; compared with Mix, data are represented as mean ± SD).

CA) in 1× TBE (25 mL) and photographed using a ChemiDoc XRS System (Bio-Rad).

Cell proliferation assay

A Cell Counting Kit-8 (CCK-8, Biorigin, Beijing, China) assay was used to evaluate the antiproliferative activity of ASO nanocomplexes (ASOs: 100 nM). HepG2 cells (1×10^4 per well) or Huh7 cells (6×10^3 per well) were seeded into 96-well plates. After incubation in a 5% CO_2, 37°C incubator for 24 h, ASO nanocomplexes were added and incubated for 48 h. NC-CT102 (NC, 5′-TCC TCG GCA GCC TGT CTA CA-3′) was used as a negative control. Then, 100 μL CCK-8 substrate was added to a 96-well plate according to the

manufacturer's protocol. The absorbance at 450 nm was measured using a microplate reader (Molecular Devices). The relative cell viability was calculated by the equation:

$$[(R_A - R_E) / (R_B - R_E)] \times 100\%$$

R_A, R_B, and R_E were defined as the absorbance of experimental samples, untreated samples and blank controls, respectively.

qRT-PCR assay

HepG2 cells were seeded into 12-well plates at a density of 1×10^5 per well (Huh7 cells, 5×10^4 per well) and cultured in a constant temperature incubator at 37°C with 5% CO_2 for 24 h. ASO nanocomplexes were added for further incubation for 24 h, and the medium was discarded. Total RNA was extracted using TRIzol Reagent (Life, Invitrogen, CA) as recommended by the manufacturer and quantified. cDNA was synthesized using a reverse transcription system (Promega, Madison, WI). Real-time PCR was performed using an Mx3005P qPCR System (Agilent) and SYBR Green qPCR Master Mix (Promega). The primer sequences used are as follows: *IGF1R* PCR Primer (forward, 5′-CTG CCT CAT TAC CTG GCT CAC TA-3′; and reverse, 5′-CAC CAT GCC ACT TTC CCT TGT-3′), β-actin PCR primer (forward, 5′-CCA ACC GCG AGA TGA-3′, and reverse, 5′-CCA GAG GCG TAC AGG GAT AG-3′). The primers were synthesized by Sangon Biotech (Shanghai, China).

Apoptosis assay

Cellular apoptosis was evaluated using an Annexin V-FITC/PI Apoptosis Detection Kit (BD, Franklin Lakes, NJ). HepG2 cells were seeded into 12-well plates at a density of 1×10^5 cells per well and grown for 24 h. The wells were treated with ASO nanocomplexes. After 24 h of transfection, the cells were detached with 0.25% trypsin (no ethylene diaminetetraacetic acid, CC034, Zhongke Maichen), washed with 4°C PBS twice, and resuspended in 100 μL of 1× binding buffer. Next, 5 μL annexin V-FITC and 5 μL PI were added to each sample, and the cells were incubated at room temperature for 20 min in the dark. The stained samples were then evaluated using a CytoFLEX instrument (Beckman Coulter, Miami, FL).

Cell uptake assay

Huh7 and HepG2 cells were seeded into 12-well plates at a density of 1×10^5 cells per well and grown for 24 h. The cells were treated with 100 nM Cy5.5-ASO nanocomplexes (or GenOpti as a control) in 10% FBS DMEM for 4 h. After that, the cells were harvested by trypsinization and centrifuged at 1,000 × *g* for 3 min, and precipitates were washed with 4°C PBS. Cellular uptake was immediately observed using a CytoFLEX instrument (Beckman Coulter).

Confocal microscopy assay

HepG2 cells were grown on 14-mm confocal observation dishes for 24 h (1×10^5 cells per well). Then, 100 nM Cy5.5-labeled ASO nanocomplexes were added to the culture medium. After incubation for 6 h in the dark, the culture medium was removed, and the cells were fixed in 4% formaldehyde for 15 min and washed twice with PBS. Cells were then stained with Hoechst 33342 (Solarbio, Beijing, China) for 20 min and observed under a Zeiss confocal microscope (Carl Zeiss MicroImaging). Confocal images were obtained using ZEN software (Carl Zeiss MicroImaging) and analyzed by ImageJ software.

Biodistribution assay

All animal experiments were approved by the Committee for Animal Research of Peking University (no. LA2017194). All animal procedures conformed to the National Institutes of Health Guide for the Care and Use of Laboratory Animals (NIH Publications no. 86-23, revised 1985). Specific pathogen-free (SPF)-grade female nude mice (4–6 weeks) were obtained from Beijing Vital River Laboratory Animal Technology (China) and kept in the Department of Laboratory Animal Science, Peking University Health Science Center.

The BALB/c-nude SPF-grade healthy female mice weighed approximately 20 g for 4–6 weeks and were randomly divided into experimental and control groups (n = 3 or 5). Each group was administered the appropriate ASO or vehicle at a dose of 1.5 mg/kg via the tail vein. The experimental group was injected with different formulations of Cy5.5-ASOs, while the control group was injected with pure solvent. Fluorescence imaging of mice was performed using an IVIS spectrum instrument (PerkinElmer) at different time points after administration. The mice were sacrificed by cervical dislocation at different time points. The heart, lung, liver, spleen, kidney, and other organs were harvested and placed on a black imaging plate. Fluorescence imaging was conducted again, and the fluorescence intensity was used to represent the amount of ASO accumulation in each organ.

Antitumor efficiency

HepG2-Luc cells (Cobioer Biosciences, Nanjing, China) *in situ* model mice were constructed by Beijing Vitalstar Biotechnology. In brief, 6-week-old female BALB/c-nu/nu nude mice were selected. HepG2-Luc cells (5×10^6) were injected into the armpit of each nude mouse. Ten days later, the axillary tumor mass was extracted and evenly divided into equal parts. Subsequently, mice were anesthetized. The liver was exposed openly, and the tumor mass was sutured to the mouse. Afterward, the wound was sutured, and mice were fed a normal diet after waking up. Two weeks later, the mice were injected intraperitoneally with the substrate D-luciferin (Yeasen Biotechnology, Shanghai, China). An IVIS spectrum instrument was used to measure the total bioluminescence flux for tumors *in vivo*. The mice with positive fluorescence staining in the liver were randomly divided into different groups and then given treatment.

Sorafenib (Aladdin, Shanghai, China) was selected as the positive control. In addition, there were the blank, CT102, $CT102_{MOE5}$, G3-$CT102_{MOE5}$, Gal-$CT102_{MOE5}$, Glu-$CT102_{MOE5}$, and Man-$CT102_{MOE5}$ groups (Table 2). After the first administration, mice in each group were intraperitoneally injected with the substrate luciferin every week and then subjected to *in vivo* imaging to observe and compare the tumor progression of the mice in each group. The weights of the mice were recorded during the whole experimental

period. Mice were dissected on the 28th day, and the effect of each AOS on tumor growth was analyzed and compared. Moreover, the peripheral blood of mice was taken, and the plasma was separated. Wuhan Service Biotechnology performed various blood biochemical tests for liver and kidney function, including AST, ALT, TBIL, BUN, and CREA tests. Frozen tumor sections from each group were prepared, and intracellular IGF1R protein expression was evaluated using immunofluorescence (Wuhan Service Biotechnology). The results were analyzed by SlideViewer and ImageJ software. Liver sections were also used for H&E staining, and the main observed lesions were photographed using a pathological slice scanner (Hamamatsu, NanoZoomer).

Western blot analysis

Total protein was extracted from whole-cell lysates using an RIPA lysis buffer kit (Thermo Scientific, Invitrogen). Equal amounts of protein samples were separated by sodium dodecyl sulfate-polyacrylamide gel electrophoresis, transferred onto polyvinylidene fluoride membranes, and the membranes were blocked with 5% nonfat milk for 1 h. The membranes were incubated with specific primary antibodies, including anti-IGF1R (ab182408, Abcam), anti-PI3K (ab32089, Abcam), anti-p-P13K (ab182651, Abcam), anti-AKT (ab18785, Abcam), and anti-p-AKT (ab38449, Abcam), at 4°C overnight. On the following day, the membranes were incubated with appropriate secondary antibodies at 37°C for 1 h. Protein bands were visualized using an enhanced chemiluminescence kit.

Human transcriptome array 2.0 transcriptome microarray analysis

Samples were submitted to Novogene. In brief, HepG2 cells were seeded in six-well plates at 1×10^6 cells per well 1 day before transfection. After the cells reached approximately 50% confluence, they were transfected with CT102, $CT102_{MOE5}$, and Glu-$CT102_{MOE5}$ nanocomplexes (ASOs: 100 nM). After incubation for 24 h, RNA was extracted from cells using TRIzol reagent according to the standard protocol. Total RNA was used as input material for the RNA sample preparations. In brief, mRNA was purified from total RNA by using poly-T oligo-attached magnetic beads. Fragmentation was carried out using divalent cations under elevated temperature in First Strand Synthesis Reaction Buffer (5×). First-strand cDNA was synthesized using random hexamer primers and M-MuLV Reverse Transcriptase, and then RNaseH was used to degrade the RNA. Second-strand cDNA synthesis was subsequently performed using DNA polymerase I and dNTP. The remaining overhangs were converted into blunt ends via exonuclease/polymerase activities. After adenylation of the 3′ ends of DNA fragments, adaptors with hairpin loop structures were ligated to prepare for hybridization. To preferentially select cDNA fragments 370–420 bp in length, the library fragments were purified with the AMPure XP system (Beckman Coulter, Beverly, CA). After PCR amplification, the PCR product was purified by AMPure XP beads, and the library was finally obtained and sequenced by the Illumina NovaSeq 6000. Differential expression analysis of two conditions/groups (two biological replicates per condition) was performed using the DESeq2R package (1.20.0).

Liquid chromatography-mass spectrometry/mass spectrometry proteomic analysis

Samples were submitted to Novogene. In brief, HepG2 cells were seeded in six-well plates at 1×10^6 cells per well 1 day before transfection. After the cells reached approximately 50% confluence, they were transfected with CT102, $CT102_{MOE5}$, and Glu-$CT102_{MOE5}$ nanocomplexes (ASOs: 100 nM). After incubation for 24 h, the cells were collected and stored at −80°C. The sample was transferred to a 1.5-mL centrifuge tube and lysed with DB lysis buffer (8 M urea, 100 mM TEAB [pH 8.5]), followed by 5 min of ultrasonication on ice. The lysate was centrifuged at 12,000 × *g* for 15 min at 4°C, and the supernatant was added to 1 M DTT and incubated for 1 h at 56°C and subsequently alkylated with sufficient iodoacetamide for 1 h at room temperature in the dark followed by an ice bath for 2 min. Tandem mass tag labeling was performed after salt removal by proteases. The separated peptides were analyzed using a Q Exactive HF-X mass spectrometer.

Statistical analysis

All data in this study are mean values from at least three independent repeated experiments, and the error line represents the standard deviation. One-way t test was used for analysis of two groups of independent data, one-way ANOVA was used for analysis of multiple groups of independent data, and p values were obtained to determine significance. GraphPad Prism 8.0 software was used for all statistical analyses.

DATA AVAILABILITY

The data that support the findings of this study are available from the corresponding author upon reasonable request.

SUPPLEMENTAL INFORMATION

Supplemental information can be found online at https://doi.org/10.1016/j.omtn.2023.04.028.

ACKNOWLEDGMENTS

This work was supported by the Ministry of Science and Technology of China (grant no. 2017ZX09303013). Industrial Funding was from Harbin Pharmaceutical Group Co., Ltd, Heilongjiang Province, China.

AUTHOR CONTRIBUTIONS

Z.Y. conceived the project, proposed constructive discussions, and supervised the research. Y.P. and J.G. designed and performed the experiments and analyzed the data. Y.P. wrote the manuscript and provided all ASO samples. Y.G., Y.Z., H.L., H.G., Q.H., and Z.G. provided experimental support. All authors contributed to the general discussion.

DECLARATION OF INTERESTS

The authors declare no competing interests.

REFERENCES

1. Bennett, C.F., Kordasiewicz, H.B., and Cleveland, D.W. (2021). Antisense drugs make sense for neurological diseases. Annu. Rev. Pharmacol. Toxicol. *61*, 831–852.
2. Wang, P., Zhou, Y., and Richards, A.M. (2021). Effective tools for RNA-derived therapeutics: siRNA interference or miRNA mimicry. Theranostics *11*, 8771–8796.
3. Le Marois, M., Tzavara, E., Ibrahim, E.C., Blin, O., and Belzeaux, R. (2021). RNA therapeutics for mood disorders: current evidence toward clinical trials. Expet Opin. Invest. Drugs *30*, 721–736.
4. Mirzaei, S., Mahabady, M.K., Zabolian, A., Abbaspour, A., Fallahzadeh, P., Noori, M., Hashemi, F., Hushmandi, K., Daneshi, S., Kumar, A.P., et al. (2021). Small interfering RNA (siRNA) to target genes and molecular pathways in glioblastoma therapy: current status with an emphasis on delivery systems. Life Sci. *275*, 119368.
5. Crooke, S.T., Liang, X.-H., Baker, B.F., and Crooke, R.M. (2021). Antisense technology: a review. J. Biol. Chem. *296*, 100416.
6. Gökirmak, T., Nikan, M., Wiechmann, S., Prakash, T.P., Tanowitz, M., and Seth, P.P. (2021). Overcoming the challenges of tissue delivery for oligonucleotide therapeutics. Trends Pharmacol. Sci. *42*, 588–604.
7. Mitchell, M.J., Billingsley, M.M., Haley, R.M., Wechsler, M.E., Peppas, N.A., and Langer, R. (2021). Engineering precision nanoparticles for drug delivery. Nat. Rev. Drug Discov. *20*, 101–124.
8. Liu, R., Luo, C., Pang, Z., Zhang, J., Ruan, S., Wu, M., Wang, L., Sun, T., Li, N., Han, L., et al. (2023). Advances of nanoparticles as drug delivery systems for disease diagnosis and treatment. Chin. Chem. Lett. *34*, 107518–107541.
9. Agrawal, S. (2021). The evolution of antisense oligonucleotide chemistry—a personal journey. Biomedicines *9*, 503–517.
10. Roberts, T.C., Langer, R., and Wood, M.J.A. (2020). Advances in oligonucleotide drug delivery. Nat. Rev. Drug Discov. *19*, 673–694.
11. Paunovska, K., Loughrey, D., and Dahlman, J.E. (2022). Drug delivery systems for RNA therapeutics. Nat. Rev. Genet. *23*, 265–280.
12. Titze-de-Almeida, S.S., Brandão, P.R.D., Faber, I., and Titze-de-Almeida, R. (2020). Leading RNA interference therapeutics part 1: silencing hereditary transthyretin amyloidosis, with a focus on Patisiran. Mol. Diagn. Ther. *24*, 49–59.
13. Akinc, A., Maier, M.A., Manoharan, M., Fitzgerald, K., Jayaraman, M., Barros, S., Ansell, S., Du, X., Hope, M.J., Madden, T.D., et al. (2019). The Onpattro story and the clinical translation of nanomedicines containing nucleic acid-based drugs. Nat. Nanotechnol. *14*, 1084–1087.
14. Eygeris, Y., Gupta, M., Kim, J., and Sahay, G. (2022). Chemistry of lipid nanoparticles for RNA delivery. Acc. Chem. Res. *55*, 2–12.
15. Guo, S., Li, K., Hu, B., Li, C., Zhang, M., Hussain, A., Wang, X., Cheng, Q., Yang, F., Ge, K., et al. (2021). Membrane-destabilizing ionizable lipid empowered imaging-guided siRNA delivery and cancer treatment. Exploration *1*, 35–49.
16. Li, C., Yang, T., Weng, Y., Zhang, M., Zhao, D., Guo, S., Hu, B., Shao, W., Wang, X., Hussain, A., et al. (2022). Ionizable lipid-assisted efficient hepatic delivery of gene editing elements for oncotherapy. Bioact. Mater. *9*, 590–601.
17. Hu, B., Li, B., Li, K., Liu, Y., Li, C., Zheng, L., Zhang, M., Yang, T., Guo, S., Dong, X., et al. (2022). Thermostable ionizable lipid-like nanoparticle (iLAND) for RNAi treatment of hyperlipidemia. Sci. Adv. *8*, eabm1418.
18. Patel, P., Ibrahim, N.M., and Cheng, K. (2021). The importance of apparent pKa in the development of nanoparticles encapsulating siRNA and mRNA. Trends Pharmacol. Sci. *42*, 448–460.
19. Dilliard, S.A., Cheng, Q., and Siegwart, D.J. (2021). On the mechanism of tissue-specific mRNA delivery by selective organ targeting nanoparticles. Proc. Natl. Acad. Sci. USA *118*. e2109256118.
20. Cheng, Q., Wei, T., Farbiak, L., Johnson, L.T., Dilliard, S.A., and Siegwart, D.J. (2020). Selective organ targeting (SORT) nanoparticles for tissue-specific mRNA delivery and CRISPR-Cas gene editing. Nat. Nanotechnol. *15*, 313–320.
21. LoPresti, S.T., Arral, M.L., Chaudhary, N., and Whitehead, K.A. (2022). The replacement of helper lipids with charged alternatives in lipid nanoparticles facilitates targeted mRNA delivery to the spleen and lungs. J. Contr. Release *345*, 819–831.
22. Berger, M., Lechanteur, A., Evrard, B., and Piel, G. (2021). Innovative lipoplexes formulations with enhanced siRNA efficacy for cancer treatment: where are we now? Int. J. Pharm. (Amst.) *605*, 120851.
23. Fehring, V., Schaeper, U., Ahrens, K., Santel, A., Keil, O., Eisermann, M., Giese, K., and Kaufmann, J. (2014). Delivery of therapeutic siRNA to the lung endothelium via novel lipoplex formulation DACC. Mol. Ther. *22*, 811–820.
24. Kulkarni, J.A., Witzigmann, D., Thomson, S.B., Chen, S., Leavitt, B.R., Cullis, P.R., and van der Meel, R. (2021). The current landscape of nucleic acid therapeutics. Nat. Nanotechnol. *16*, 630–643.
25. Zhang, M.M., Bahal, R., Rasmussen, T.P., Manautou, J.E., and Zhong, X.B. (2021). The growth of siRNA-based therapeutics: updated clinical studies. Biochem. Pharmacol. *189*, 114432.
26. Aimo, A., Castiglione, V., Rapezzi, C., Franzini, M., Panichella, G., Vergaro, G., Gillmore, J., Fontana, M., Passino, C., and Emdin, M. (2022). RNA-targeting and gene editing therapies for transthyretin amyloidosis. Nat. Rev. Cardiol. *19*, 655–667. https://doi.org/10.1038/s41569-022-00683-z.
27. Springer, A.D., and Dowdy, S.F. (2018). GalNAc-siRNA conjugates: leading the way for delivery of RNAi therapeutics. Nucleic Acid Therapeut. *28*, 109–118.
28. Cui, H., Zhu, X., Li, S., Wang, P., and Fang, J. (2021). Liver-targeted delivery of oligonucleotides with N-Acetylgalactosamine conjugation. ACS Omega *6*, 16259–16265.
29. Ranasinghe, P., Addison, M.L., Dear, J.W., and Webb, D.J. (2022). Small interfering RNA (siRNA): discovery, pharmacology and clinical development - an introductory review. Br. J. Pharmacol. https://doi.org/10.1111/bph.15972.
30. Debacker, A.J., Voutila, J., Catley, M., Blakey, D., and Habib, N. (2020). Delivery of oligonucleotides to the liver with GalNAc: from research to registered therapeutic drug. Mol. Ther. *28*, 1759–1771.
31. Min, H.S., Kim, H.J., Naito, M., Ogura, S., Toh, K., Hayashi, K., Kim, B.S., Fukushima, S., Anraku, Y., Miyata, K., and Kataoka, K. (2020). Systemic brain delivery of antisense oligonucleotides across the blood-brain barrier with a glucose-coated polymeric nanocarrier. Angew Chem. Int. Ed. Engl. *59*, 8173–8180.
32. Nahar, U.J., Toth, I., and Skwarczynski, M. (2022). Mannose in vaccine delivery. J. Contr. Release *351*, 284–300.
33. O'Sullivan, J., Muñoz-Muñoz, J., Turnbull, G., Sim, N., Penny, S., and Moschos, S. (2022). Beyond GalNAc! Drug delivery systems comprising complex oligosaccharides for targeted use of nucleic acid therapeutics. RSC Adv. *12*, 20432–20446.
34. Patra, M., Johnstone, T.C., Suntharalingam, K., and Lippard, S.J. (2016). A potent glucose-platinum conjugate exploits glucose transporters and preferentially accumulates in cancer cells. Angew Chem. Int. Ed. Engl. *55*, 2550–2554.
35. Zhou, T., Peng, J., Hao, Y., Shi, K., Zhou, K., Yang, Y., Yang, C., He, X., Chen, X., and Qian, Z. (2021). The construction of a lymphoma cell-based, DC-targeted vaccine, and its application in lymphoma prevention and cure. Bioact. Mater. *6*, 697–711.
36. Ruan, S., Qin, L., Xiao, W., Hu, C., Zhou, Y., Wang, R., Sun, X., Yu, W., He, Q., and Gao, H. (2018). Acid-responsive transferrin dissociation and GLUT mediated exocytosis for increased blood–brain barrier transcytosis and programmed glioma targeting delivery. Adv. Funct. Mater. *28*, 1802227.
37. Lin, R.X., Wang, Z.Y., Zhang, N., Tuo, C.W., Liang, Q.D., Sun, Y.N., and Wang, S.Q. (2007). Inhibition of hepatocellular carcinoma growth by antisense oligonucleotides to type I insulin-like growth factor receptor *in vitro* and in an orthotopic model. Hepatol. Res. *37*, 366–375.
38. Zhou, X., Pan, Y., Yu, L., Wu, J., Li, Z., Li, H., Guan, Z., Tang, X., and Yang, Z. (2021). Feasibility of cRGD conjugation at 5'-antisense strand of siRNA by phosphodiester linkage extension. Mol. Ther. Nucleic Acids *25*, 603–612.
39. Ma, Y., Zhao, W., Li, Y., Pan, Y., Wang, S., Zhu, Y., Kong, L., Guan, Z., Wang, J., Zhang, L., and Yang, Z. (2019). Structural optimization and additional targets identification of antisense oligonucleotide G3139 encapsulated in a neutral cytidinyl-lipid combined with a cationic lipid *in vitro* and *in vivo*. Biomaterials *197*, 182–193.
40. Li, L., Long, J., Sang, Y., Wang, X., Zhou, X., Pan, Y., Cao, Y., Huang, H., Yang, Z., Yang, J., and Wang, S. (2021). Rational preparation and application of a mRNA delivery system with cytidinyl/cationic lipid. J. Contr. Release *340*, 114–124.

41. Wu, J., Wang, S., Li, X., Zhang, Q., Yang, J., Ma, Y., Guan, Z., and Yang, Z. (2021). Selective anti-melanoma effect of phosphothioated aptamer encapsulated by neutral cytidinyl/cationic lipids. Front. Cell Dev. Biol. *9*, 660233.

42. Zhou, X., Pan, Y., Li, Z., Li, H., Wu, J., Ma, Y., Guan, Z., and Yang, Z. (2020). siRNA packaged with neutral cytidinyl/cationic/PEG lipids for enhanced antitumor efficiency and safety *in vitro* and *in vivo*. ACS Appl. Bio Mater. *3*, 6297–6309.

43. Ma, Y., Zhu, Y., Wang, C., Pan, D., Liu, S., Yang, M., Xiao, Z., Yang, X., Zhao, W., Zhou, X., et al. (2018). Annealing novel nucleobase-lipids with oligonucleotides or plasmid DNA based on H-bonding or pi-pi interaction: assemblies and transfections. Biomaterials *178*, 147–157.

44. Guan, J., Pan, Y., Li, H., Zhu, Y., Gao, Y., Wang, J., Zhou, Y., Guan, Z., and Yang, Z. (2022). Activity and tissue distribution of antisense oligonucleotide CT102 encapsulated with cytidinyl/cationic lipid against hepatocellular carcinoma. Mol. Pharm. *19*, 4552–4564.

45. Keating, M.F., Drew, B.G., and Calkin, A.C. (2022). Antisense oligonucleotide technologies to combat obesity and fatty liver disease. Front. Physiol. *13*, 839471.

46. Hill, S.F., and Meisler, M.H. (2021). Antisense oligonucleotide therapy for neurodevelopmental disorders. Dev. Neurosci. *43*, 247–252.

47. Tarn, W.Y., Cheng, Y., Ko, S.H., and Huang, L.M. (2021). Antisense oligonucleotide-based therapy of viral infections. Pharmaceutics *13*, 2015.

48. Paunovska, K., Sago, C.D., Monaco, C.M., Hudson, W.H., Castro, M.G., Rudoltz, T.G., Kalathoor, S., Vanover, D.A., Santangelo, P.J., Ahmed, R., et al. (2018). A direct comparison of *in vitro* and *in vivo* nucleic acid delivery mediated by hundreds of nanoparticles reveals a weak correlation. Nano Lett. *18*, 2148–2157.

49. Baimanov, D., Wang, J., Zhang, J., Liu, K., Cong, Y., Shi, X., Zhang, X., Li, Y., Li, X., Qiao, R., et al. (2022). In situ analysis of nanoparticle soft corona and dynamic evolution. Nat. Commun. *13*, 5389.

50. Hong, C., Liang, J., Xia, J., Zhu, Y., Guo, Y., Wang, A., Lu, C., Ren, H., Chen, C., Li, S., et al. (2020). One stone four birds: a novel liposomal delivery system multi-functionalized with ginsenoside Rh2 for tumor targeting therapy. Nano-Micro Lett. *12*, 129.

51. Petrov, R.A., Mefedova, S.R., Yamansarov, E.Y., Maklakova, S.Y., Grishin, D.A., Lopatukhina, E.V., Burenina, O.Y., Lopukhov, A.V., Kovalev, S.V., Timchenko, Y.V., et al. (2021). New small-molecule glycoconjugates of docetaxel and GalNAc for targeted delivery to hepatocellular carcinoma. Mol. Pharm. *18*, 461–468.

52. Kim, Y., Jo, M., Schmidt, J., Luo, X., Prakash, T.P., Zhou, T., Klein, S., Xiao, X., Post, N., Yin, Z., and MacLeod, A.R. (2019). Enhanced potency of GalNAc-conjugated antisense oligonucleotides in hepatocellular cancer models. Mol. Ther. *27*, 1547–1557.

53. Ma, W.K., Voss, D.M., Scharner, J., Costa, A.S.H., Lin, K.T., Jeon, H.Y., Wilkinson, J.E., Jackson, M., Rigo, F., Bennett, C.F., and Krainer, A.R. (2022). ASO-based PKM splice-switching therapy inhibits hepatocellular carcinoma growth. Cancer Res. *82*, 900–915.

54. Fu, H.W., Lin, X., Zhu, Y.X., Lan, X., Kuang, Y., Wang, Y.Z., Ke, Z.G., Yuan, T., and Chen, P. (2019). Circ-IGF1R has pro-proliferative and anti-apoptotic effects in HCC by activating the PI3K/AKT pathway. Gene *716*, 144031.

55. Armas, P., David, A., and Calcaterra, N.B. (2017). Transcriptional control by G-quadruplexes: *In vivo* roles and perspectives for specific intervention. Transcription *8*, 21–25.

56. Pelechano, V., and Steinmetz, L.M. (2013). Gene regulation by antisense transcription. Nat. Rev. Genet. *14*, 880–893.

57. Crooke, S.T., Wang, S., Vickers, T.A., Shen, W., and Liang, X.H. (2017). Cellular uptake and trafficking of antisense oligonucleotides. Nat. Biotechnol. *35*, 230–237.

58. Nedorezova, D.D., Dubovichenko, M.V., Belyaeva, E.P., Grigorieva, E.D., Peresadina, A.V., and Kolpashchikov, D.M. (2022). Specificity of oligonucleotide gene therapy (OGT) agents. Theranostics *12*, 7132–7157.